Geophysical Journal International

Geophys. J. Int. (2020) **223,** 348–365
Advance Access publication 2020 June 19
GJI Seismology

doi: 10.1093/gji/ggaa306

Modelling of pulse-like velocity ground motion during the 2018 M_w 6.3 Hualien earthquake, Taiwan

Yen-Yu Lin [1,2] Hiroo Kanamori,[3] Zhongwen Zhan,[3] Kuo-Fong Ma[1,2,4] and Te-Yang Yeh[5,6]

[1] *Department of Earth Sciences, National Central University, Taoyuan* 32001, *Taiwan. E-mail: yenyulin@cc.ncu.edu.tw*
[2] *Earthquake-Disaster & Risk Evaluation and Management Center, National Central University, Taoyuan* 32001, *Taiwan*
[3] *Seismological Laboratory, California Institute of Technology, Pasadena, CA* 91125, *USA*
[4] *Institute of Earth Sciences, Academia Sinica, Taipei* 11529, *Taiwan*
[5] *Department of Geological Sciences, San Diego State University, San Diego, CA* 92182-1020, *USA*
[6] *Scripps Institution of Oceanography, University of California San Diego, La Jolla, CA* 92093, *USA*

Accepted 2020 June 15. Received 2020 June 4; in original form 2020 February 19

SUMMARY

The 2018 February 6 M_w 6.3 Hualien earthquake caused severe localized damage in Hualien City, located 20 km away from the epicentre. The damage was due to strong (>70 cm s^{-1}) and sharp (duration ∼2.5 s) velocity pulses. The observed peak ground-motion velocity in Hualien City symmetrically decays with distance from the nearby Milun fault. Waveforms observed on the opposite sides of the fault show reversed polarity on the vertical and N–S components while the E–W component is almost identical. None of the published finite-fault slip models can explain the spatially highly localized large velocity pulses. In this study, we show that an M_w 5.9 strike-slip subevent on the Milun fault at 2.5 km depth, rupturing from north to south at ∼0.9*V*s speed, combined with site effects caused by surficial layers with low S-wave speed, can explain the velocity pulses observed at the dense strong-motion network stations. This subevent contributes only 25 per cent of the total moment of the 2018 Hualien earthquake, suggesting that a small local slip patch near a metropolis can dominate the local hazard. Our result strongly suggests that seismic hazard assessments should consider large ground-motion variabilities caused by directivity and site effects, as observed in the 2018 Hualien earthquake.

Key words: Earthquake ground motions; Earthquake source observations; Site effects.

1 Introduction

On 2018 February 6, a moderate-size event (M_w 6.3) occurred offshore eastern Taiwan at a depth of 6.3 km [Central Weather Bureau (CWB), Fig. 1]. This earthquake, hereafter called the 2018 Hualien earthquake, caused 17 deaths, 295 injuries and 25 collapsed/damaged buildings in Hualien City, located 20 km to the south of the epicentre (Fig. 1b). The area with high peak ground velocity (PGV) is concentrated in a 5 × 5 km^2 section of Hualien City, which coincides with the heavily damaged area (Fig. 2), but is different from the high peak ground acceleration (PGA) area near the epicentre (Fig. 1a). The concentration of the damage zone caused by this moderate-size earthquake surprised the community. The estimated centroid location of the 2018 Hualien earthquake determined by the real-time moment tensor (RMT) monitoring system (Lee *et al.* 2013) is close to Hualien City (Fig. 1b). Two nodal planes of the mechanism diagram are dipping to the west and to the south with high angles (Lee *et al.* 2019). The 1951 M_L 7.1 Hualien earthquake, which occurred in the same area as the 2018 event, also caused serious damage in Hualien City. It appears that both events occurred in the same seismogenic structure.

The rupture process of the 2018 Hualien earthquake appears to be complex. Lee *et al.* (2019) used three geophysical data sets—teleseismic, local ground-motion waveforms and Global Positioning System (GPS) co-seismic displacements—to investigate the source properties of the 2018 Hualien earthquake. They found that the rupture propagated from the hypocentre in the north towards the south into a steeply west-dipping fault plane at a depth of 8∼10 km, then jumped to a shallower east-dipping fault near Hualien City, called the Milun fault. The aftershocks of the 2018 Hualien earthquake clearly delineate the large west-dipping fault (Kuo-Chen *et al.* 2019), but its tectonic interpretation is still debated. Wen *et al.* (2019) determined a kinematic source model using teleseismic waveforms and GPS displacements, and also concluded that two fault segments are necessary for this earthquake. The slip pattern is similar to that proposed by Lee *et al.* (2019); the rupture propagated from north to south and the largest slip occurred near Hualien City. Yang *et al.* (2018) obtained a similar pattern of slip

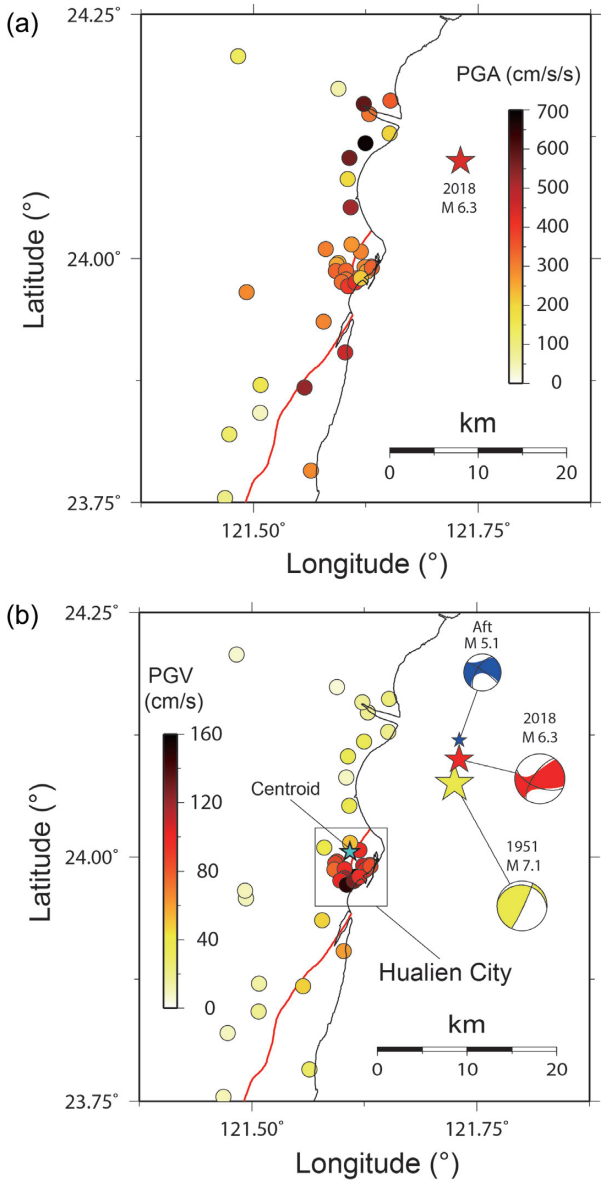

Figure 1. (a) Distribution of the observed PGA during the 2018 Hualien earthquake. Circles are strong-motion stations with the PGA in colour. The red star indicates the epicentre of the 2018 Hualien earthquake. (b) Distribution of the observed PGV during the 2018 Hualien earthquake. Circles are the strong-motion stations with the PGV in colour. The hypocentre and focal mechanism of the 1951 Hualien earthquake, 2018 Hualien earthquake and the aftershock of the 2018 event (Aft) are shown by stars and beach balls, respectively. The light blue star indicates the centroid location of the 2018 event from the RMT solution. The black box indicates the area in Fig. 2.

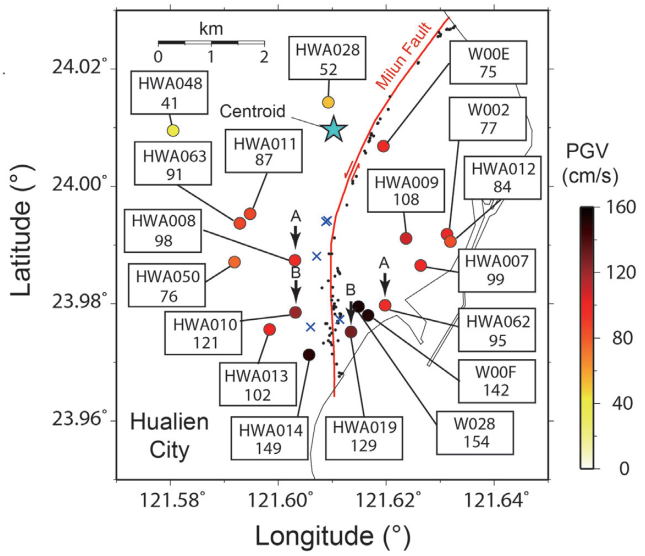

Figure 2. Distribution of the observed PGV in Hualien City. The station name and its PGV are shown in the figure. The red line indicates the surface rupture of the Milun fault. The black dots and blue crosses are the surface fractures and collapsed buildings recognized by the geological survey (CGS 2018). The light blue star is the centroid location of the 2018 event. The arrows A and B indicate the station pairs A and B for waveform comparison in Fig. 6.

asperities using geodetic data (i.e. GPS and InSAR) and estimated the dip angles of the unknown west-dipping fault and the east-dipping Milun fault as ∼85.2° and ∼72°, respectively. Huang & Huang (2018) combined seismic data, geodetic data, and levelling measurements, and suggested that this earthquake may have started on a conjugate fault with an E–W strike in the hypocentre, then triggered slips on the unknown west-dipping fault and the Milun fault. The largest slip was located on the Milun fault. Lo *et al.* (2019) considered three curved segments for the 2018 Hualien earthquake and employed teleseismic, regional strong motion, SAR, and GPS data in a joint inversion to constrain the kinematic rupture process of the 2018 Hualien earthquake. The slip pattern is similar to that of the other source models. The modelling results of Yen *et al.* (2019) also suggest a heterogeneous slip pattern and fault system.

The rupture and damage patterns of the 2018 Hualien earthquake along the Milun fault are quite similar to those of the 1951 Hualien earthquake. Furthermore, the directivity of the 2018 event is significant towards the south from the epicentre (Jian *et al.* 2019; Lee *et al.* 2019; Wen *et al.* 2019). The shake map from the early warning system supports this source characteristic (Wu *et al.* 2019).

These studies all agree that the 2018 Hualien earthquake occurred on several fault segments. A small subevent, Sub-1, is located near the hypocentre reported by CWB, and a larger subevent, Sub-2, is at the centroid location determined by RMT near Hualien City (Fig. 3a). On the N–S record section of the velocity records from P-alert, we can see P- and S-phase moveouts on the locally normalized record section in Fig. 3(b). The globally normalized record section shows larger amplitude and lower frequency seismic signals from Sub-2 (Fig. 3c). We roughly estimate the source parameters of Sub-1 in Appendix A and Fig. A1. Sub-1 is an M_w 5.6 event with nodal planes with strike dip, and rake of 211°/62°/−8° and 305°/82°/207° determined by comparing its waveforms to that of an M_w 5.1 aftershock (Aft) that occurred near the hypocentre. Thus, Sub-1 is only a small part of the 2018 Hualien earthquake, and M_w of Sub-2 (nominally, $M_w = 6.27$) is essentially the same as that of the 2018 Hualien earthquake as a whole.

Rupture directivity effect causes high amplitude ground motions in the forward direction of rupture propagation with a short local slip duration (Ben-Menahem 1961, 1962; Lay & Wallace 1995; Somerville *et al.* 1997). Strong pulse-like velocity ground motion (hereafter, shortened to velocity pulse) with a duration of ∼2.5 s was recorded by strong motion stations near the Milun fault as shown in Figs 4(a) and A2. These pulses are believed to be responsible for the damage in Hualien City. The largest PGV and peak ground-motion displacement (PGD) are 154 cm s^{-1} and 83 cm, respectively, which were recorded at W028. Kuo *et al.* (2019) suggested that the collapse

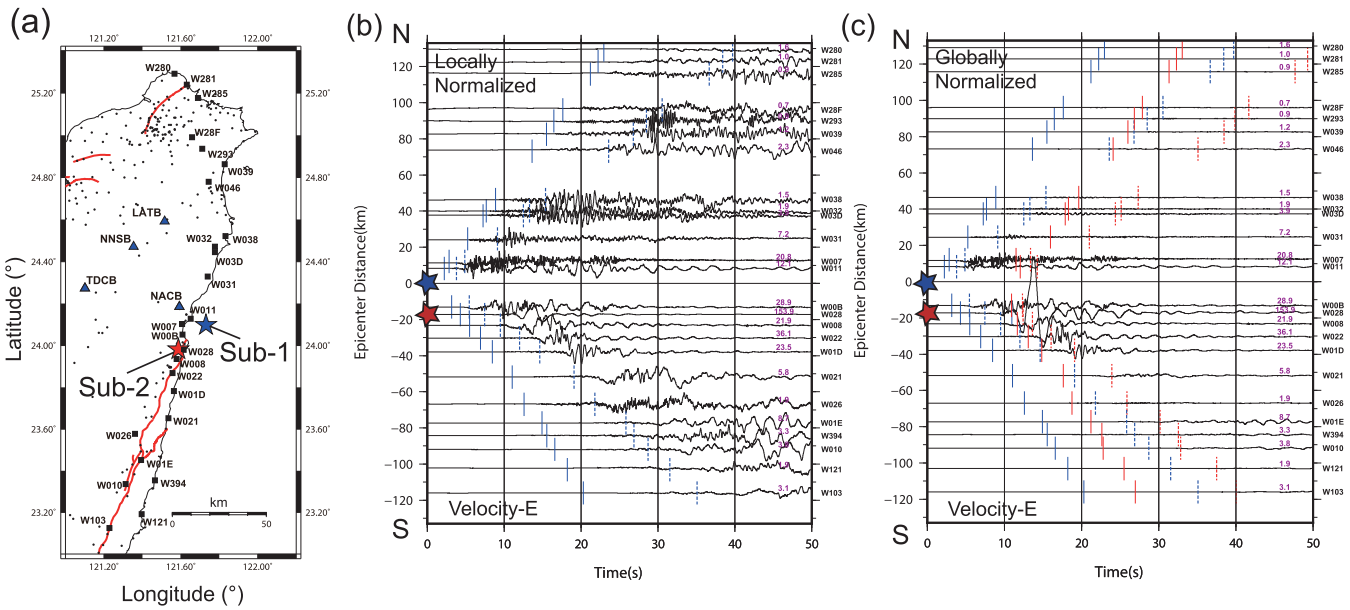

Figure 3. (a) Distribution of the P-alert stations (squares) used for the record section in (b). The triangles indicate the stations of Broadband Array in Taiwan for Seismology used to determine the source parameters of Sub-1 in Appendix A. (b) The N–S record section of velocity for the 2018 Hualien earthquake. The predicted arrival times for *P* and *S* waves generated by Sub-1 at the hypocentre (blue star) are shown by blue solid and dashed bars, respectively. The amplitude is normalized to the maximum amplitude of each trace. (c) The record section with the amplitudes normalized to the maximum amplitude of all the traces. The predicted arrival times for *P* and *S* waves generated by Sub-2 at the hypocentre (red star) are shown by red solid and dashed bars, respectively. The long-period arrivals are the *S* waves from Sub-2.

of four buildings may have been influenced by site amplification at a period of 1 s. According to a report of the field investigation by Central Geological Survey, Taiwan (CGS 2018), all surface ruptures and damaged structures were along the Milun fault, shown in Fig. 2, suggesting that the slip on the Milun fault was possibly responsible for the velocity pulse. However, this is still being debated because the published slip models suggest that the slips were spread on several faults (Huang & Huang 2018; Yang *et al.* 2018; Lee *et al.* 2019; Wen *et al.* 2019).

The significant impact of pulse-like velocity ground motions on earthquake damage has been observed for several earthquakes (e.g. 1994 Northridge, 1995 Kobe, 1999 Chi-Chi and 2016 Meinong earthquakes). This subject is important in earthquake engineering since the combination of velocity and displacement pulses could heavily damage structures, especially tall buildings (Hall *et al.* 1995). Several studies suggested that the pulse is generated by near-fault forward directivity (Somerville *et al.* 1997; Somerville 2003; Baker 2007; Shahi & Baker 2011). According to Cox & Ashford (2002), three conditions are required for producing a large velocity pulse: (1) The earthquake is larger than M_w 6.0, (2) The site is within 10 km of a fault and (3) The rupture propagates towards the site.

2 Large discrepancy of the ground-motion amplitude near the Milun fault between the observed and predicted from slip inversion models

Almost all the papers on the 2018 Hualien earthquake we referenced are concerned with the extensive damage in the city of Hualien caused by the anomalously large velocity pulses. However, we found no clear demonstration of how anomalous the observed velocity pulses are. A better understanding of the cause of the anomalously large pulses is important for planning effective seismic hazard mitigation measures, especially in Taiwan.

As mentioned earlier, several other investigators performed slip inversions using seismic data (e.g. Huang & Huang 2018; Lee *et al.* 2019; Lo *et al.* 2019; Wen *et al.* 2019). However, Huang & Huang (2018) used only broad-band seismic data recorded on bedrock sites. Wen *et al.* (2019) used only teleseismic data. Lo *et al.* (2019) used regional strong-motion records but not those near the Milun fault. Lee *et al.* (2019) applied teleseismic and regional records but considered only the Z-component waveform of the strong-motion records near the Milun fault. Since the amplitudes of the strong-motion records near the Milun fault are locally so large that unless the detailed fault geometry near the Milun fault and the Green's functions with extremely high spatial resolution are available, it is not possible to properly handle these records in a single inversion scheme. Thus, these records were left unexplained in these studies. Since such a multiscale inversion study is not feasible at present, we perform a forward modelling as a best alternative.

The most detailed slip inversion study by Lee *et al.* (2019) compared the velocity ground-motion amplitudes between the observed and predicted by their model in their fig. S-3, reproduced in Fig. 5(a). As shown in Fig. 5(a), the observed ground motion at two stations near the Milun fault HWA060 and HWA028 (in red boxes) are much larger than predicted by their slip model that can explain not only teleseismic but also most regional data well. Their model includes deep and shallow slip near the Milun fault (fig. 2 of Lee *et al.* 2019). We note that the observed ground motions close to the Milun fault at HWA062 and HWA008 (in blue box) are even larger than that at HWA060, by a factor of 4 as shown in Fig. 5(b). Although Lee *et al.* (2019) did not show the predicted ground motion at HWA062 and HWA008, judging from the general trend of the predicted amplitude in the area, their slip model most likely underpredicts the amplitude at HWA062 and HWA008 by at least an order of magnitude. Lee *et al.* (2019) pointed out that this under-estimation could be due to

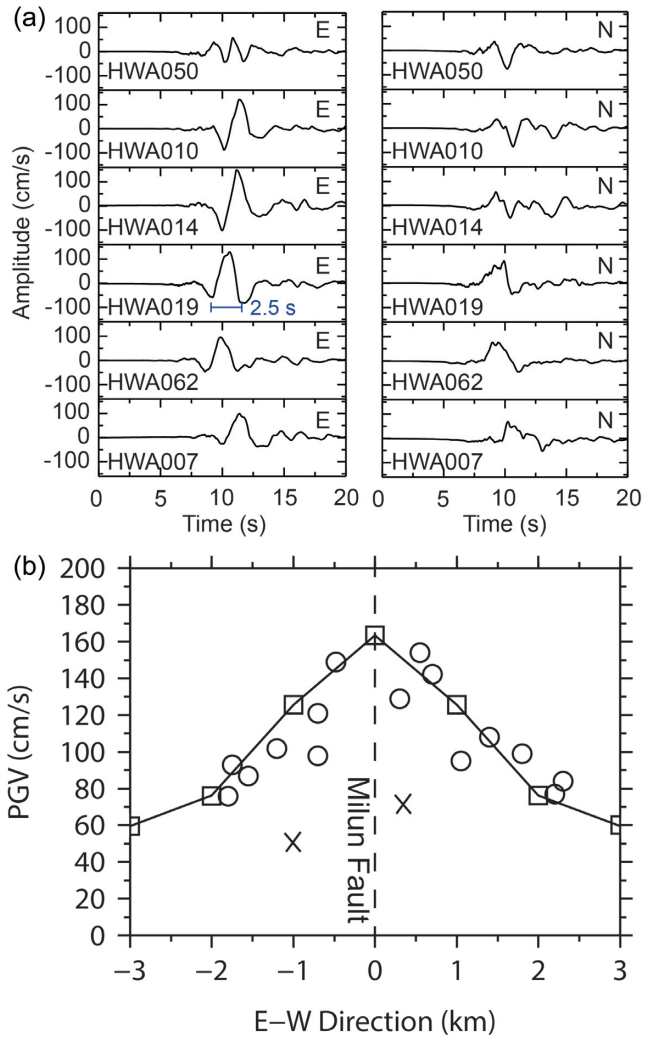

Figure 4. (a) The pulse-like ground motion observed in Hualien City. (b) Comparison of the observed and simulated PGVs plotted as a function of distance to the Milun fault in Hualien City. The circles and squares are the observations and simulated results, respectively. Two crosses indicate outliers from the stations HWA028 and W00E near the northern part of the Milun fault.

strong site effects. This observation strongly suggests that a very local source with strong directivity and large site effects is required to explain the anomalously large velocity pulses near the Milun fault.

3 Data

We focus on the local strong motion networks in Hualien City (Fig. 2) that recorded the pulse-like velocity ground motion. These networks are: (1) the Taiwan Strong Motion Instrumentation Program (TSMIP) network managed by CWB and (2) the P-alert network for the early warning system developed by National Taiwan University (Wu *et al.* 2013, 2019). The TSMIP and P-alert instruments are accelerometers. The instrument response of P-alert is flat in acceleration between 0.07 and 10 Hz. The instruments of TSMIP have a broader plateau of instrument response from DC to 50 Hz (Liu *et al.* 1999; Liu & Tsai 2005). The sampling rates are 100 and 200 samples per second for P-alert and TSMIP stations, respectively. Clocks used for P-alert instruments are controlled by the Network Time Protocol through the Internet. Clocks of some of the TSMIP instruments are not calibrated, however. We did not use the arrival time information from the TSMIP stations. We discarded records with large drift or clipping.

4 Modelling the pulse-like velocity ground motion of the 2018 Hualien earthquake

Our detailed examination of the ground motion near the Milun fault shows two distinct features. As shown in Fig. 4(b) and Table 1, the PGV decays with distance from the Milun fault in a symmetric pattern; this can be most naturally explained if the Milun fault is near vertical at a shallow depth. This structure may appear somewhat different from the generally held view on geological ground (Shyu *et al.* 2016) that the Milun fault dips at 75° to a depth of 10 km. However, it is possible that the shallowest part of the Milun fault is nearly vertical. There are two outliers of PGV in Fig. 4(b) at the stations HWA028 and W00E in the northern Milun fault. These stations are not located exactly in the forward direction of rupture propagation, and the amplification effect is not as large as that for the stations to the south.

Another notable feature is shown in Fig. 6. Two pairs of stations on opposite sides of the Milun fault shown in Fig. 2(a) exhibit intriguing symmetry: while the E–W component waveforms are similar, the vertical and the N–S component waveforms are reversed in polarity.

To explore a model causing the observed features, we model the velocity pulse near Hualien in detail using a simple fault model and the waveforms recorded at the densely distributed stations near the Milun fault. Our model is a line source 7 km long consisting of 11 subevents shown in Fig. 7(a). We adjust the magnitude and focal mechanism of the subevents as well as the rupture speed and direction of the line source to obtain the simplest source model for explaining the observed pulse-like ground motion. Using the *F–K* integration method (Zhu & Rivera 2002), we compute synthetic waveforms at virtual stations distributed uniformly on the surface with a 1 km interval in both N–S and E–W directions. The sampling rate of the simulations is 20 points s^{-1} and a wave number increment $dk = 0.005\ m^{-1}$ is used for simulation. We tested simulations with smaller dk to make sure that the synthetic waveforms remain unchanged, as shown in Fig. A3. We use an average 1-D velocity structure taken from a Taiwan 3-D velocity structure in the Hualien region (Huang *et al.* 2014), and include the site effect with a low-velocity structure (Lin *et al.* 2018a) on top of the 1-D structure; we call this structure the soft strucutre (Table 2).

After testing many models, we obtain the best source model with a series of M_w 5.2 subevents with a triangular source-time function with a duration of ∼2.3 s occurring at a depth of 2.5 km. The magnitude and duration of the entire fault are M_w 5.9 and ∼5 s, respectively (Fig. 7b). The directivity is from north to south with a rupture speed of 2.36 km s^{-1} (∼0.9*V*s) (Fig. 7a). The focal mechanism of all the subevents is a vertical left-lateral strike-slip (strike = 180°, dip = 90°, and rake = 0°). Tests for various dip angles for the subevents are shown in Figs A4 and A5.

This model can reproduce the seismograms recorded at the strong motion sites in Hualien City. (1) The stations with high computed PGV are concentrated south of the line source shown in Fig. 8(c) due to the strong directivity towards the south. (2) The computed PGV decreases rapidly with distance from the line source due to the near-field effect. This pattern is consistent with the observations shown in Fig. 4(b). (3) The computed velocity and displacement waveforms at a station pair south of the line source, one station on

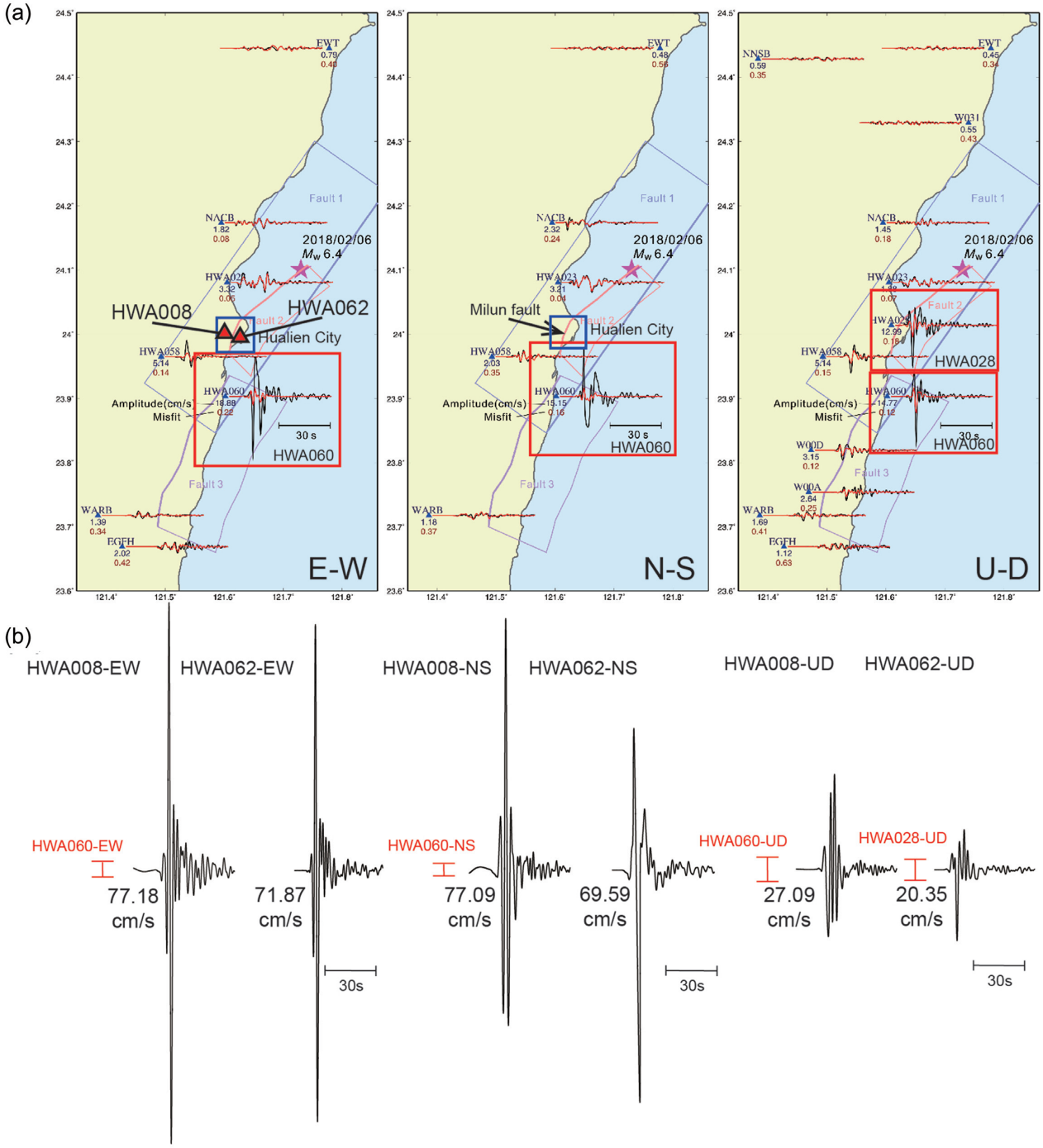

Figure 5. (a) Comparison of the inversion results by Lee *et al.* (2019) with the observed. The black and red lines show the observations and the synthetics. The blue boxes are the research area of this study. The red boxes show the areas where the waveform comparisons at the stations near Hualien City (HWA028 and HWA060) shown in the study of Lee *et al.* (2019) are made. The left, middle and right sections show the E–W, N–S and U–D components, respectively. This figure is modified from fig. S-3 in Lee *et al.* (2019). (b) The observed waveforms used in this study at the stations HWA062 and HWA008 in Hualien City. The amplitude scale is the same as that for (a). The red vertical bars indicate the peak-to-trough amplitudes predicted by Lee *et al.*'s (2019) model at stations HWA060 and HWA028. The records were filtered with a 0.05–0.5 Hz passband. The PGV for each waveform is marked on the figure.

the west side of it (Station W) and the other on the east side (Station E), produce the reversed polarity pattern shown in Figs 8(a) and (b). (4) The PGV (∼150 cm s^{-1}) and PGD (∼70 cm) are similar between the synthetics and the observed (Fig. 6). (5) The duration of the computed pulse, approximately 2.5 s, shown in Fig. 8(a) is similar to the observations shown in Fig. 4(a). Our modelling suggests that the directivity effect and proximity to the fault are the most important factors for generating the pulse-like velocity ground motion near Hualien.

Our objective is to explain the observed extremely large amplitudes rather than the detailed waveforms. However, it is of interest to see to what extent the waveforms computed with a very simple

Table 1. Observed PGV and distance of stations to the Milun fault.

Station	W–E distance (km)	PGV (cm s^{-1})
HWA048	− 3.50	41
HWA050	− 1.80	76
HWA063	− 1.75	91
HWA011	− 1.55	87
HWA013	− 1.20	102
HWA028	− 1.00	52
HWA010	− 0.70	121
HWA008	− 0.70	98
HWA014	− 0.48	149
HWA019	0.30	129
W00E[a]	0.35	75
W028[a]	0.55	154
W00F[a]	0.70	142
HWA062	1.05	95
HWA009	1.40	108
HWA007	1.80	99
W002[a]	2.20	77
HWA012	2.30	84

[a]Stations of the P-alert network.

forward modelling compare with the observed. To this end, we compare the ground-motion records at stations HWA014 and HWA019, located on the west and east side of the Milun fault, respectively, near the southern end (Fig. 2), with the synthetics computed for the virtual sites, W and E (Fig. 8). Since we do not know the exact location of the slip zone and the southern extent of the Milne fault, the exact timing is unknown. Thus, we aligned the observed and synthetic records at the largest motion on the E–W (fault-normal) component. Fig. A6 shows the results. Since our modelling is only forward without knowing the details of the fault geometry, the details are not expected to match. Nevertheless, we consider the overall agreement of the waveforms satisfactory, suggesting that our rupture model is reasonable. We note some phase mismatch on the minor N–S component. Since the stations near the end of the fault like HWA014 and HWA019 are nodal for the N–S component, some complications are expected.

If we assume that the vertical width of the fault is approximately 5 km, we obtain the average slip of the line source to be ∼85 cm using the relation $M_0 = \mu \bar{D} S$ (we use $\mu = 30$ GPa as the average rigidity). This is comparable to the average co-seismic slip on the surface, ∼50 cm, estimated from the GPS measurements (Huang & Huang 2018).

Thus, we suggest that an M_w ∼5.9 subevent on the Milun fault at a shallow depth (∼2.5 km) with directivity towards the south can be the primary cause of the velocity pulse observed in Hualien. This subevent, which we call Sub-2-Milun, is a part of Sub-2 described earlier in this paper and in several other studies (Lee *et al.* 2019; Wen *et al.* 2019). The magnitude of Sub-2-Milun depends on the assumed focal depth, which is not constrained well. Since $M_w = 5.9$ is much smaller than the $M_w = 6.27$ of Sub-2, the shallow slip is only a small part of the slip of Sub-2, and more slip must have occurred on the deeper part of the Milun fault and the west-dipping unknown fault (Lee *et al.* 2019). The difference in the moment between the $M_w = 6.27$ and $M_w = 5.9$ events is 2.3×10^{18} Nm ($M_w = 6.18$). According to the finite fault model proposed by Lee *et al.* (2019), most slips of Sub-2 occurred on the west-dipping deeper fault near the centroid location reported by the RMT solution.

As we discussed in Section 2, the ground motion at the stations near the Milun Fault (e.g. HWA008) predicted by the slip model of Lee *et al.* (2019) is probably very small compared with the observed. However, since the details are still unknown, we test two deep slip models as an alternative way to assess the contribution of the deeper slip to the observed slip pulse. First, we compute ground motions at the site of HWA014 for a point source with the RMT mechanism at the RMT location (depth = 8 km, $M_w = 6.18$ and duration = 6 s). The result is shown in Fig. 9(a). The PGV produced by this point source is only 16 cm s^{-1}, which is only ∼10 per cent of the observed PGV (∼150 cm s^{-1}). Second, to test the effect of directivity towards south, we compute ground motion at the site of HWA014 by moving the proposed line source from a depth of 2.5 to 8.0 km with a rupture velocity of 2.92 km s^{-1} (0.9Vs). The magnitude is increased to M_w 6.18. The result is shown in Fig. 9(b). The PGV for this deeper event is only 27 cm s^{-1}, which is only 18 per cent of the observed PGV. From these tests, we conclude that the contribution from the deeper source is insignificant.

Our model is based on forward modelling and is not unique. The actual fault geometry, rupture speed, rise time and the crustal structure are likely more complex. However, given the limited information on the fault geometry and 3-D crustal structure, more detailed modelling is not warranted, but our simple model hopefully captures the general features of rupture in the shallow part of the Milun fault. Our point is to show that a relatively small shallow fault can produce destructive velocity pulses under certain conditions.

5 Discussion

5.1 Directivity and proximity of fault

We showed that an M_w 5.9 Sub-2-Milun with a 7 km long line source alone can produce the observed velocity pulse near Hualien City, although the 2018 Hualien earthquake as a whole occurred on a much larger complex fault system. Other subevents did not contribute much to the generation of the velocity pulse because they were far away from the high PGV area. The M_w 5.9 Sub-2-Milun with $M_0 = 8.81 \times 10^{17}$ N m contributes only 25 per cent of the total seismic moment 3.51×10^{18} N m of the M_w 6.3 Hualien earthquake. However, this small amount of seismic moment could be responsible for the major damage in Hualien City. Ground motions produced by the nearby subfaults can be more significant than those generated by faults on structures deeper and farther away. The lesson we learn from the 2018 Hualien earthquake is that we have to pay more attention to active faults near large cities even if they are short (e.g. Milun fault).

The factors responsible for the velocity pulse during the 2018 Hualien earthquake, directivity and proximity of the source fault to the sites, are the essential conditions proposed by Cox & Ashford (2002). The occurrence of the largest velocity pulse on the E–W component, which is perpendicular to the rupture direction from north to south, is also consistent with the predicted characteristics of the velocity pulse (Cox & Ashford 2002), and the one observed in Hualien City is a typical example.

5.2 Site effect

To test the contribution of the site effect to amplification of the velocity pulse, we compare the synthetic waveforms computed with the 1-D velocity model with (soft), and without (hard), a shallow low-velocity structure listed in Tables 2 and 3, respectively. The results are shown in Figs 8(a) and 10(a). PGV for the soft and hard structures are ∼120 and ∼40 cm s^{-1}, respectively, indicating that the site effect is important for amplification. However, the shape of

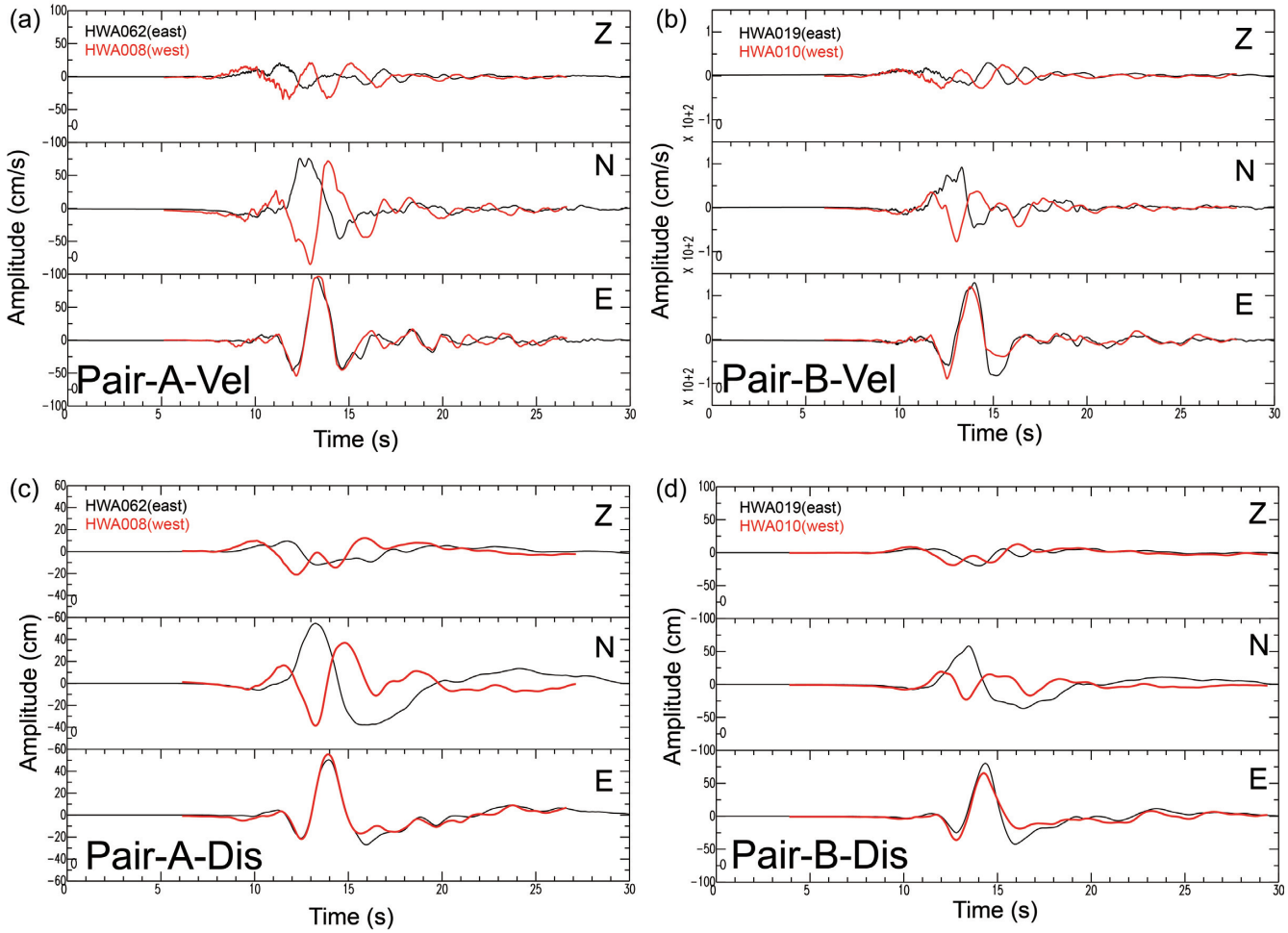

Figure 6. Comparison of the waveforms observed on the west and east sides of the Milun fault in Hualien City. (a and b) The velocity records for the station pairs A and B marked in Fig. 2. The black and red waveforms show the records observed east and west of the Milun fault, respectively. (c and d) Similar to (a) and (b) with the displacement records. Note the polarity reversal for the Z and N–S components between the east and west sides.

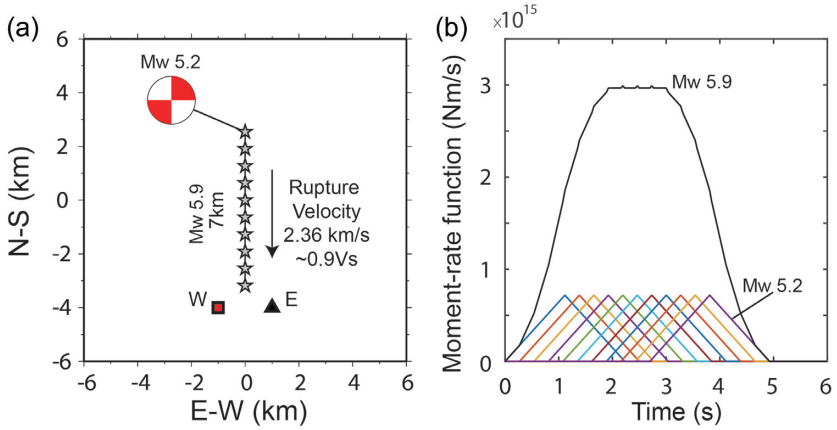

Figure 7. Modelling of the pulse-like ground motion near the Milun fault. (a) A line source with 11 M_w 5.2 subevents. All events are with a pure left-lateral strike-slip mechanism. The rupture velocity is 2.36 km s^{-1}. The red square and blue triangle show a virtual station pair. (b) The moment-rate functions of the line source and each subevent.

the waveforms for the soft and hard structures is similar (Figs 8a and 10a), suggesting that the site effect has minor influence on the duration of the velocity pulse. The duration of the pulse is mainly controlled by the source properties (e.g. source geometry, rupture velocity and directivity).

Wang *et al.* (2018), Kuo *et al.* (2019), Yamada *et al.* (2019) and Miyakoshi *et al.* (2019) reported that Vs30 (average *S*-wave speed in the top 30 m) is different between the east and west side of the Milun fault. From fig. 7 of Wang *et al.* (2018), we estimate that Vs30 = 300 and 580 m s^{-1} for the west and east side of the Milun

Table 2. 1-D velocity structure near Hualien City (Soft).

Thickness (km)	Vp (km s^{-1})	Vs (km s^{-1})	Density (g cm^{-3})	Qp	Qs
0.2	2.40	0.70	2.0	60	30
0.2	3.40	1.13	2.2	60	30
0.8	4.20	1.52	2.3	60	30
1.0	4.20	1.90	2.4	60	30
2.5	4.21	2.55	2.6	600	300
3.0	4.89	2.95	2.6	600	300
4.0	5.58	3.24	2.6	600	300
5.0	5.87	3.41	2.6	600	300
5.0	6.14	3.56	2.6	600	300
5.0	6.44	3.70	2.6	600	300
5.0	6.71	3.82	2.6	600	300
5.0	6.96	3.97	2.6	600	300
5.0	7.19	4.12	2.6	600	300
5.0	7.45	4.24	2.6	600	300
5.0	7.63	4.32	2.6	600	300
5.0	7.78	4.42	2.6	600	300

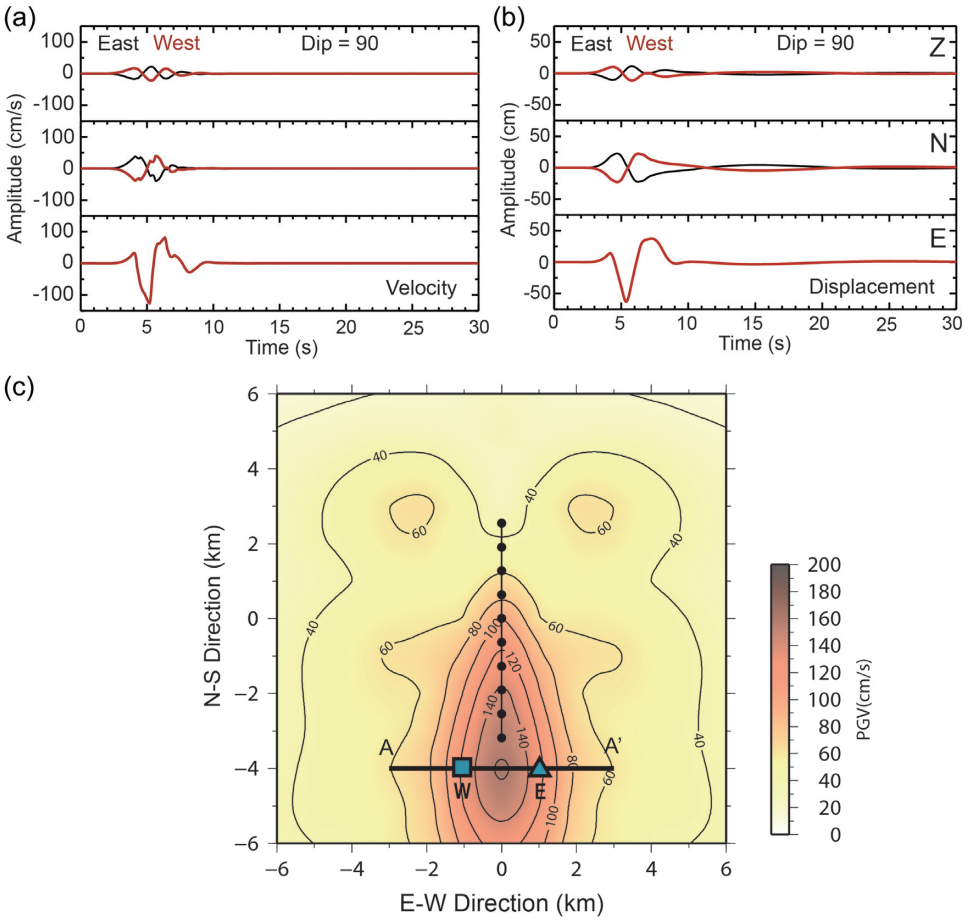

Figure 8. (a) The simulated velocity and (b) displacement waveforms for the station pair showing the waveforms with reversed polarity in the Z and N–S components and the same polarity in the E–W component. (c) Distribution of the simulated PGV in colour for the line source. The black line shows the A-A' profile with PGV shown in Fig. 4(b). The black dots and black line depict the line source shown in Fig. 7(a).

fault, respectively. Thus, we consider these structures by modifying the top 30 m of the soft structure shown in Table 2 (Tables 4 and 5). As shown in Fig. 10(b), no significant difference in the waveform and amplitude between the east and the west side. The waveforms and amplitudes shown in Fig. 10(b) are also similar to those shown in Fig. 8(a) (the soft structure). Thus, the contrast in Vs30 between the east and the west side of the Milun fault does not significantly affect the amplitude of the velocity pulses with a period of about 2 s. However, as we can see in these figures, Vs30 may have some effects on high-frequency accelerations.

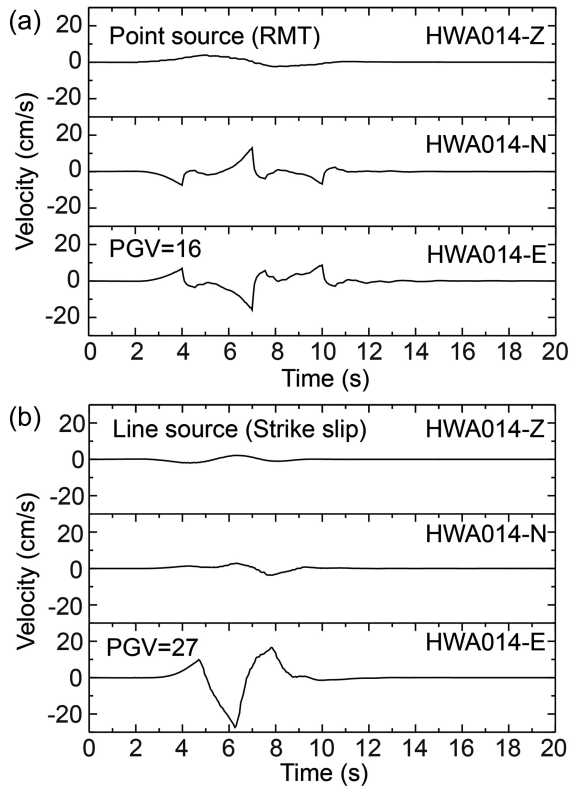

Figure 9. (a) The synthetic waveforms for a point source at RMT location (deeper event). The PGV value is written on the figure. (b) The synthetic waveforms for a line source with directivity at a depth of 8 km.

5.3 Complex slip patches in moderate earthquakes

A complex slip pattern similar to that of the 2018 Hualien earthquake was found for the M_w 6.2 Meinong earthquake, Taiwan, in 2016. This earthquake had a small M_w 5.3 subevent at the hypocentre that triggered a larger subevent with M_w 6.18 at 12 km north-northwest of the epicentre. The combination of the strong directivity, proximity of the M_w 6.18 subevent to Tainan city in southern Taiwan, and site effects was responsible for the strong velocity pulse (PGV $>$ 70 cm s^{-1}) and caused serious damage in Tainan City (Lee *et al.* 2016; Lin *et al.* 2018b). The 2018 Hualien earthquake and the 2016 Meinong earthquake are similar in several respects. (1) Both events were moderate events with distinct subevents. (2) The initial subevent (M_w ~5) at the hypocentre was smaller but triggered a larger subevent(s) (M_w ~6) 10–20 km away. (3) The later subevent generated the velocity pulse with a high PGV ($>$ 70 cm s^{-1}) causing heavy damage and casualties. (4) The velocity pulse was caused mainly by directivity, proximity of the later subevent to a metropolis, and site effects. To have several subevents (asperities) distributed on a fault is a common feature of seismic faulting. It is important to investigate the interaction between the subevents and understand the mechanisms of rupture growth. Seismic waveforms recorded by a dense network of strong motion stations near the source region provide important information of the details of the rupture process.

One difference of the source properties between the 2016 Meinong and the 2018 Hualien earthquakes in generating the velocity pulse is the size of the key subevent. The subevent in the 2016 Meinong earthquake was M_w 6.18 and contributed 93 per cent of the total seismic moment (Lin *et al.* 2018b). However, Sub-2-Milun of the 2018 Hualien earthquake was only 25 per cent. This difference indicates that the key subevent is not necessarily the largest. The location (proximity) and rupture direction (directivity) can be more critical.

5.4 Implication for the 1951 Hualien earthquake

The historical M_L 7.1 Hualien earthquake occurred on 22 October, 1951, offshore in eastern Taiwan (Cheng *et al.* 1997) close to the 2018 Hualien earthquake location (Fig. 1b). Chen *et al.* (2008) estimated the M_w of this earthquake to be 6.6 using the M_L–M_w relation. Geological surveys indicated a 2 m co-seismic surface offset on the Milun fault in 1951 (CGS 2018). Since this is much larger than the maximum surface offset of ~50 cm observed for the 2018 Hualien earthquake, it is possible that the 1951 event produced an even larger velocity pulse than that (a maximum of ~150 cm s^{-1}) of the 2018 Hualien earthquake. A practical solution for mitigation of hazards caused by the velocity pulse is to regulate construction of structures along the Milun fault.

5.5 Contribution to seismic hazard assessment

Our result underscores the importance of site-specific seismic hazard assessment (SHA) for effectively dealing with the situations like that involving the Milun fault and the city of Hualien. SHA is a commonly used technique for analysing seismic hazard (e.g. ground-motion prediction equation). In general, probabilistic seismic hazard assessment (PSHA) is made for designing structures and buildings for public use. In these general approaches, it is difficult to consider directivity effect of a source since the probabilities for different combinations of rupture direction and the rupture initiation point are unknown and cannot be incorporated in a physical model. Hence, earthquakes with strong directivity which produces extremely high PGA, PGV, and spectral acceleration (SA) become outliers (e.g. 1999 Chi-Chi, 2016 Meinong, and 2018 Hualien earthquakes). To deal with this situation, engineers and seismologists should apply deterministic seismic hazard assessment (DSHA) for designing important structures and buildings (e.g. tall apartment buildings, nuclear power plants and dams). All possible scenarios for a nearby target fault including directivity, proximity of fault, and site effects must be evaluated for designing the target structures.

6 Conclusions

The pulse-like velocity ground motion with a high amplitude ($>$ 70 cm s^{-1}) and a short duration (~2.5 s) during the 2018 M_w 6.3 Hualien earthquake that caused heavy damage and casualties in Hualien City 20 km away from the hypocentre has several distinct features: (1) The stations with high PGV are concentrated in a 5 × 5 km^2 area near the southern end of the Milun fault; (2) Observed PGV rapidly decays with distance from the Milun fault over 3 km; and (3) The observed waveforms, both velocity and displacement, from the opposite sides of the Milun fault show opposite polarity on the vertical and N–S components, but are almost identical on the E–W component. None of the published fault slip models determined with finite-fault slip inversion methods can explain the spatially highly localized large velocity pulses, because the area of the large amplitudes is very localized.

To explain the observed seismic signatures, we forward modelled the waveforms recorded at the densely distributed stations near the Milun fault using a simple fault model. The distinct features of the velocity pulse described above can be produced by a local M_w 5.9

Table 3. 1-D velocity structure near Hualien City (Hard).

Thickness (km)	Vp (km s^{-1})	Vs (km s^{-1})	Density (g cm^{-3})	Qp	Qs
0.5	3.57	2.09	2.6	600	300
2.5	4.21	2.55	2.6	600	300
3.0	4.89	2.95	2.6	600	300
4.0	5.58	3.24	2.6	600	300
5.0	5.87	3.41	2.6	600	300
5.0	6.14	3.56	2.6	600	300
5.0	6.44	3.70	2.6	600	300
5.0	6.71	3.82	2.6	600	300
5.0	6.96	3.97	2.6	600	300
5.0	7.19	4.12	2.6	600	300
5.0	7.45	4.24	2.6	600	300
5.0	7.63	4.32	2.6	600	300
5.0	7.78	4.42	2.6	600	300

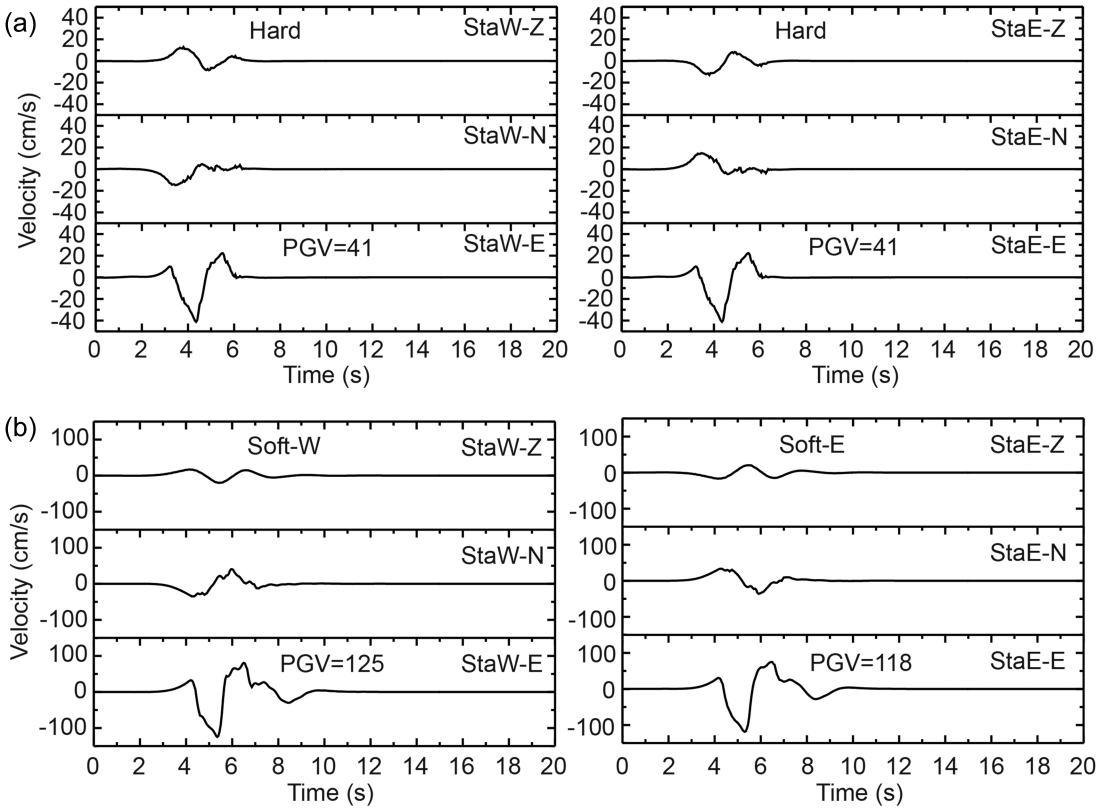

Figure 10. (a) The synthetic waveforms for the line source at a depth of 2.5 km on the west (left-hand figures) and east (right-hand figures) sides of the Milun fault. The 'hard' structure without shallow low velocity layers (Table 3) is used. The PGV values are written on the figure. (b) The synthetic waveforms for the line source at a depth of 2.5 km on both sides of the Milun fault. Different Vs30 structure on top of the soft structure is used for the west (Soft-W) and east sides (Soft-E) (Tables 4 and 5).

subevent on the Milun fault (Sub-2-Milun). Although this subevent contributes only 25 per cent of the total seismic moment of the 2018 Hualien event, the directivity effect and its proximity to the site are the key factors for generating the large velocity pulse. The site effect is also important for amplification of the pulse by a factor of 3. Slips on a local patch near a metropolis may dominate the hazard. Our result suggests that seismic hazard assessments should consider the ground-motion variabilities due to strong directivity effects such as those observed during the 2018 Hualien earthquake.

ACKNOWLEDGEMENTS

We appreciate the helpful comments from the Editor, Prof. Jean Virieux, two referees, Mr Hugo Samuel Sánchez-Reyes and Anonymous. We thank Dr Hsin-Hua Huang and Dr Shiann-Jong Lee for providing us with the Taiwan 3-D velocity structure and the earthquake source parameters determined with the Real-Time Moment Tensor Monitoring System, respectively. We thank the Central Weather Bureau for providing us with the TSMIP records and source parameters, including the location and focal mechanism of

Table 4. 1-D velocity structure near Hualien City (Soft-E).

Thickness (km)	Vp (km s^{-1})	Vs (km s^{-1})	Density (g cm^{-3})	Qp	Qs
0.015	2.10	0.50	2.0	60	30
0.185	2.40	0.70	2.0	60	30
0.2	3.40	1.13	2.2	60	30
0.8	4.20	1.52	2.3	60	30
1.0	4.20	1.90	2.4	60	30
2.5	4.21	2.55	2.6	600	300
3.0	4.89	2.95	2.6	600	300
4.0	5.58	3.24	2.6	600	300
5.0	5.87	3.41	2.6	600	300
5.0	6.14	3.56	2.6	600	300
5.0	6.44	3.70	2.6	600	300
5.0	6.71	3.82	2.6	600	300
5.0	6.96	3.97	2.6	600	300
5.0	7.19	4.12	2.6	600	300
5.0	7.45	4.24	2.6	600	300
5.0	7.63	4.32	2.6	600	300
5.0	7.78	4.42	2.6	600	300

Table 5. 1-D velocity structure near Hualien City (Soft-W).

Thickness (km)	Vp (km s^{-1})	Vs(km s^{-1})	Density(g cm^{-3})	Qp	Qs
0.03	2.00	0.30	2.0	60	30
0.17	2.40	0.70	2.0	60	30
0.2	3.40	1.13	2.2	60	30
0.8	4.20	1.52	2.3	60	30
1.0	4.20	1.90	2.4	60	30
2.5	4.21	2.55	2.6	600	300
3.0	4.89	2.95	2.6	600	300
4.0	5.58	3.24	2.6	600	300
5.0	5.87	3.41	2.6	600	300
5.0	6.14	3.56	2.6	600	300
5.0	6.44	3.70	2.6	600	300
5.0	6.71	3.82	2.6	600	300
5.0	6.96	3.97	2.6	600	300
5.0	7.19	4.12	2.6	600	300
5.0	7.45	4.24	2.6	600	300
5.0	7.63	4.32	2.6	600	300
5.0	7.78	4.42	2.6	600	300

the 2018 Hualien earthquake. We thank Prof. Yih-Min Wu at National Taiwan University for providing the Palert records. We thank Dr Che-Min Lin at the National Center for Research on Earthquake Engineering who provided us with the shallow structure for Hualien City. We thank Dr Chung-Han Chan, Mr Jia-Cian Gao, and Dr Chun-Hsiang Kuo for helpful discussion in seismic hazard assessment. This research was supported by the Taiwan Earthquake Research Center (TEC), funded through the Ministry of Science and Technology (Taiwan) with grant number MOST 108–2116-M-008–025-MY2. The TEC contribution number for this article is 00159. This work is financially supported by 'Earthquake-Disaster & Risk Evaluation and Management Center, E-DREaM' from The Featured Areas Research Center Program within the framework of the Higher Education Sprout Project by the Ministry of Education (MOE) in Taiwan. Z. Zhan is supported by the U.S. Geological Survey under grant number G19AP00030.

The strong-motion records used in this study were obtained from the National Taiwan University (NTU), the Institute of Earth Sciences (IES) of Academia Sinica and the Central Weather Bureau (CWB). The P-alert records used in this study are available to the public and can be downloaded from the NTU cloud disk (http://palert.earth.sinica.edu.tw/db/, last accessed October 2019). The strong-motion records from IES and CWB used in this study can be obtained upon request from IES and CWB. The damage records used in this study are at http://fault.moeacgs.gov.tw/MgFault/index.php/10–2017-06–02-07–05-29/130–1070330 (last accessed October 2019). The moment tensors determined with Broadband Array in Taiwan for Seismology (BATS) solution are available at http://bats.earth.sinica.edu.tw (last accessed October 2019). The Central Weather Bureau (CWB) website can be accessed at http://www.cwb.gov.tw/eng/index.htm (last accessed October 2019). Seismic Analysis Code (SAC) is available at http://ds.iris.edu/files/sac-manual/(last accessed October 2019). Frequency-Wavenumber (FK) synthetic seismogram package is available at http://www.eas.slu.edu/People/LZhu/home.html (last accessed October 2019).

References

Baker, J.W., 2007. Quantitative classification of near-fault ground motions using wavelet analysis, *Bull. seism. Soc. Am.,* **97**(5), 1486–1501.

Ben-Menahem, A., 1961. Radiation of seismic surface-waves from finite moving sources, *Bull. seism. Soc. Am.,* **51**(3), 401–435.
Ben-Menahem, A., 1962. Radiation of seismic body waves from a finite moving source in the earth, *J. geophys. Res.,* **67**(1), 345–350.
CGS, 2018. Report of the 20180206 Hualien earthquake and geologic survey, Central Geology Survey, pp. 115 (in Chinese). Retrieved from http://esrpc.ncu.edu.tw/public/tw/news/detail/852/0.
Cheng, S.N., Yu, T.T., Yeh, Y.T. & Chang, Z.S., 1997. Relocation of the 1951 Hualien, Taitung earthquake sequence, in *Proceedings of Meteorology, Conference on Weather Analysis and Forecasting,* pp. 690–699, Central Weather Bureau, Taipei, Taiwan.
Chen, K.H., Toda, S. & Rau, R.J., 2008. A leaping, triggered sequence along a segmented fault: The 1951 ML 7.3 Hualien-Taitung earthquake sequence in eastern Taiwan, *J. geophys. Res.,* **113**(B2) B02304, doi:10.1029/2007JB005048.
Cox, K.E. & Ashford, S.A., 2002. Characterization of large velocity pulses for laboratory testing, Report 2002/22, Pacific Earthquake Engineering Research Center, University of California, Berkeley, California, USA.
Hall, J.F., Heaton, T.H., Halling, M.W. & Wald, D.J., 1995. Near-source ground motion and its effects on flexible buildings, *Earthq. Spectra,* **11**(4), 569–605.
Huang, H.H., Wu, Y.M., Song, X., Chang, C.H., Lee, S.J., Chang, T.M. & Hsieh, H.H., 2014. Joint Vp and Vs tomography of Taiwan: Implications for subduction-collision orogeny, *Earth planet. Sci. Lett.,* **392,** 177–191.
Huang, M.H. & Huang, H.H., 2018. The complexity of the 2018 Mw 6.4 Hualien earthquake in east Taiwan, *Geophys. Res. Lett.,* **45**(24), 13–249.
Jian, P.R., Hung, S.H. & Meng, L., 2019. Rupture behavior and interaction of the 2018 Hualien earthquake sequence and its tectonic implication, *Seismol. Res. Lett.,* **90**(1), 68–77.
Kuo, C.H., Huang, J.Y., Lin, C.M., Hsu, T.Y., Chao, S.H. & Wen, K.L., 2019. Strong ground motion and pulse-like velocity observations in the near-fault region of the 2018 Mw 6.4 Hualien, Taiwan, earthquake, *Seismol. Res. Lett.,* **90**(1), 40–50.
Kuo-Chen, H., Guan, Z.K., Sun, W.F., Jhong, P.Y. & Brown, D., 2019. Aftershock sequence of the 2018 M_w 6.4 Hualien earthquake in eastern Taiwan from a dense seismic array data set, *Seismol. Res. Lett.,* **90**(1), 60–67.
Lay, T. & Wallace, T.C., 1995. *Modern Global Seismology,* Vol. 58, Elsevier.
Lee, S.J., Lin, T.C., Liu, T.Y. & Wong, T.P., 2019. Fault-to-fault jumping rupture of the 2018 M_w 6.4 Hualien earthquake in eastern Taiwan, *Seismol. Res. Lett.,* **90**(1), 30–39.
Lee, S.J., Yeh, T.Y. & Lin, Y.Y., 2016. Anomalously large ground motion in the 2016 ML 6.6 Meinong, Taiwan, earthquake: A synergy effect of source rupture and site amplification, *Seismol. Res. Lett.,* **87**(6) 1319–1326.
Lee, S.J. *et al.*, 2013. Towards real-time regional earthquake simulation I: real-time moment tensor monitoring (RMT) for regional events in Taiwan, *Geophys. J. Int.,* **196**(1), 432–446.
Lin, C.M., Kuo, C.H., Huang, J.Y., Hsieh, H.H., Si, C.C. & Wen, K.L., 2018a, Shallow shear-wave velocity structures of TSMIP stations in Taiwan, NCREE-18-019, technical report (in Chinese), pp. 141.
Lin, Y.Y., Yeh, T.Y., Ma, K.F., Song, T.R.A., Lee, S.J., Huang, B.S. & Wu, Y.M., 2018b. Source characteristics of the 2016 Meinong (M_L 6.6), Taiwan, earthquake, revealed from dense seismic arrays: double sources and pulse-like velocity ground motion, *Bull. seism. Soc. Am.,* **108**(1), 188–199.
Liu, K.S., Shin, T.C. & Tsai, Y.B., 1999. A free-field strong motion network in Taiwan: TSMIP, *Terr. Atmos. Ocean. Sci.,* **10**(2), 377–396.
Liu, K.S. & Tsai, Y.B., 2005. Attenuation relationships of peak ground acceleration and velocity for crustal earthquakes in Taiwan, *Bull. seism. Soc. Am.,* **95**(3), 1045–1058.
Lo, Y.C., Yue, H., Sun, J., Zhao, L. & Li, M., 2019. The 2018 Mw6. 4 Hualien earthquake: dynamic slip partitioning reveals the spatial transition from mountain building to subduction, *Earth planet. Sci. Lett.,* **524,** 115729.
Miyakoshi, K. *et al.*, 2019. *Estimation of Underground Structures around Source Area of the 2018 Hualien Earthquake (Mw 6.4) using Microtremor Array Observations*. Paper presented at 2019 Seismological Society of Japan Fall Meeting, Naha, Japan, (in Japanese).
Shahi, S.K. & Baker, J.W., 2011. An empirically calibrated framework for including the effects of near-fault directivity in probabilistic seismic hazard analysis, *Bull. seism. Soc. Am.,* **101**(2), 742–755.
Shyu, J.B.H., Chuang, Y.R., Chen, Y.L., Lee, Y.R. & Cheng, C.T., 2016. A new on-land seismogenic structure source database from the Taiwan Earthquake Model (TEM) Project for seismic hazard analysis of Taiwan, *Terr. Atmos. Ocean. Sci.,* **27**(3), 311–323.
Somerville, P.G., 2003. Magnitude scaling of the near fault rupture directivity pulse, *Phys. Earth planet. Inter.,* **137**(1-4), 201–212.
Somerville, P.G., Smith, N.F., Graves, R.W. & Abrahamson, N.A., 1997. Modification of empirical strong ground motion attenuation relations to include the amplitude and duration effects of rupture directivity, *Seismol. Res. Lett.,* **68**(1), 199–222.
Wang, X., Si, H., Koketsu, K., Nagano, M. & Dang, J., 2018. *Building Damage, Strong Ground Motion Characteristics and Indoor*. Paper presented at the 15th Japan Earthquake Engineering Symposium, Sendai, Japan, (in Japanese).
Wen, Y.Y., Wen, S., Lee, Y.H. & Ching, K.E., 2019. The kinematic source analysis for 2018 M_w 6.4 Hualien, Taiwan earthquake. *Terr. Atmos. Ocean. Sci.,* **30,** 1–11.
Wu, Y.M., Chen, D.Y., Lin, T.L., Hsieh, C.Y., Chin, T.L., Chang, W.Y., Li., W.S. & Ker, S.H., 2013. A high-density seismic network for earthquake early warning in Taiwan based on low cost sensors, *Seismol. Res. Lett.,* **84**(6), 1048–1054.
Wu, Y.M., Mittal, H., Huang, T.C., Yang, B.M., Jan, J.C. & Chen, S.K., 2019. Performance of a low-cost earthquake early warning system (P-Alert) and shake map production during the 2018 M_w 6.4 Hualien, Taiwan, earthquake, *Seismol. Res. Lett.,* **90**(1), 19–29.
Yamada, M. *et al.*, 2019. *Strong Motions and Estimation of the Subsurface Soil Structure for the 2018 Hualien Earthquake in Taiwan*. Paper presented at 2019 Japan Geoscience Union Meeting, Chiba, Japan, (in Japanese).
Yang, Y.H. *et al.*, 2018. Co-seismic and postseismic fault models of the 2018 M_w 6.4 Hualien earthquake occurred in the junction of collision and subduction boundaries offshore Eastern Taiwan, *Remote Sens.,* **10**(9), 1372, doi:10.3390/rs10091372.
Yen, J.Y. *et al.*, 2019. Insights into seismogenic deformation during the 2018 Hualien, Taiwan, earthquake sequence from InSAR, GPS, and modeling, *Seismol. Res. Lett.,* **90**(1), 78–87.
Zhu, L. & Rivera, L.A., 2002. A note on the dynamic and static displacements from a point source in multilayered media, *Geophys. J. Int.,* **148**(3), 619–627.

APPENDIX A

A1 Source properties of Sub-1

Since Sub-2 occurred to the south of Sub-1 (Fig. 3) with a delay, it is possible to study the source properties of Sub-1 by using records in the northern stations without using the waveforms generated by Sub-2. We found an aftershock with M_w 5.1 near the hypocentre of the 2018 Hualien earthquake (Fig. 1b). This event, called Aft, occurred at 18:00 (UTC) on 2018 February 6 and its direct *S* waveforms are similar to those of Sub-1 (Fig. A1). The similarity of the broad-band waveforms for stations NNSB, LATB, TDCB and NACB suggests that Sub-1 and Aft have a similar mechanism. The two nodal planes reported by RMT are (strike/dip/rake) = (228°/82°/15°) and (305°/82°/207°). We further estimate the magnitude of Sub-1 by comparing the amplitude at these four stations. The average of the amplitudes' ratio of Sub1 to Aft is 8.6, indicating that the magnitude difference between the two events is M_w ~0.5. Thus, the magnitude of Sub-1 is estimated to be M_w ~5.6 ($M_0 = 3.13 \times 10^{17}$ N m).

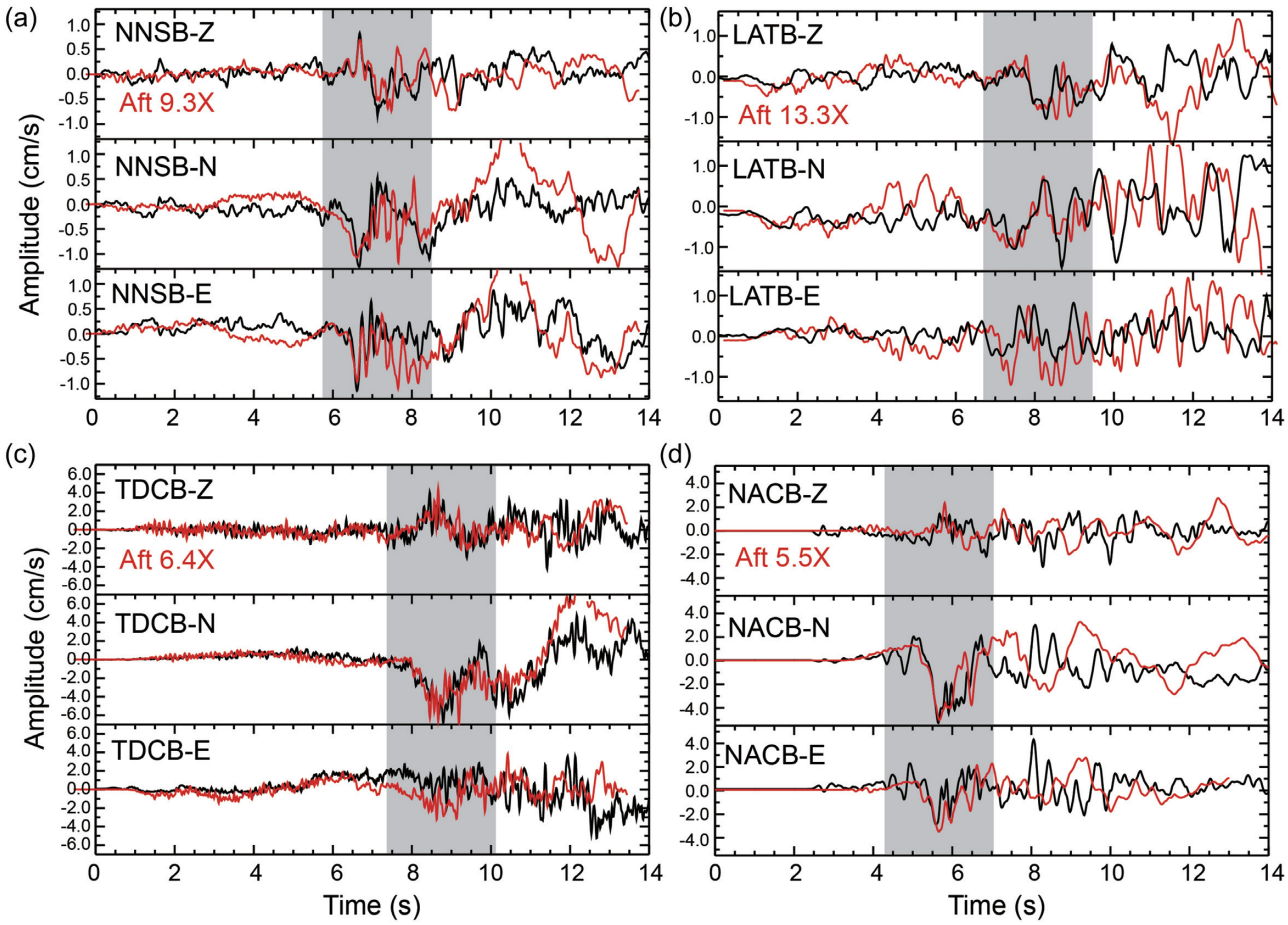

Figure A1. Comparison of the waveforms recorded by four BATS stations (a) NNSB, (b) LATB, (c) TDCB and (d) NACB between Sub-1 and Aft. The red waveforms are from Aft with the factor of amplification marked on the figures. The black waveforms are from the 2018 Hualien earthquake. The grey areas indicate the waveforms of the direct *S* wave.

APPENDIX B

B1 Observed velocity pulse on the east and west sides of the Milun fault

Fig. A2 shows observed velocity records on the east and west sides of the Milun fault.

APPENDIX C

C1 Test for a different wavenumber increment (dk) used in the *F–K* simulation

Fig. A3 compares synthetic waveforms computed with dk = 0.005 m^{-1} and dk = 0.001 m^{-1}. dk = 0.005 m^{-1} is sufficiently small for accurate computation.

APPENDIX D

D1 Effect of dip angle and rake angle on the waveforms

To test the effect of dip angle and rake angle on the waveforms on the N–S and Z components observed on the east and west sides of the Milun fault, we computed synthetic displacements with variable dip angles of 60°, 70° and 80° towards the east in Fig. A4 and towards the west in Fig. A5. We also consider rake angles 0° and 30°, because Huang & Huang (2018) showed from GPS measurements that the slip on the Milun fault had larger horizontal than vertical movements. The results indicate that the dip angle of the Milun fault should be larger than 80° for generating the reversed polarity of the waveforms recorded on the east and west of the fault. We cannot resolve the dip direction from the local strong motion records. This means that the Milun fault is a nearly vertical fault at least at a shallow depth. The rake angles seem to be irrelevant to the observed polarity reversal pattern.

APPENDIX E

E1 Comparisons of the observed and synthetic waveforms near the southern end of the Milun fault

Fig. A6 demonstrates comparisons between the observed and synthetic velocity waveforms near the southern end of the Milun fault.

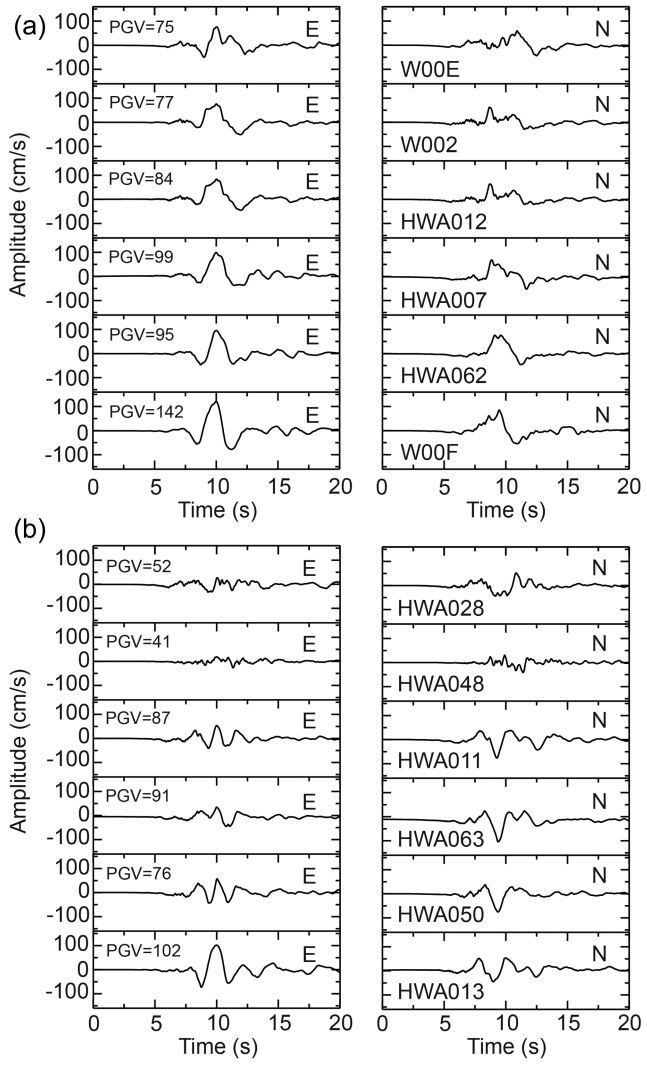

Figure A2. Observed velocity records on the east side (a) and the west side (b) of the Milun fault.

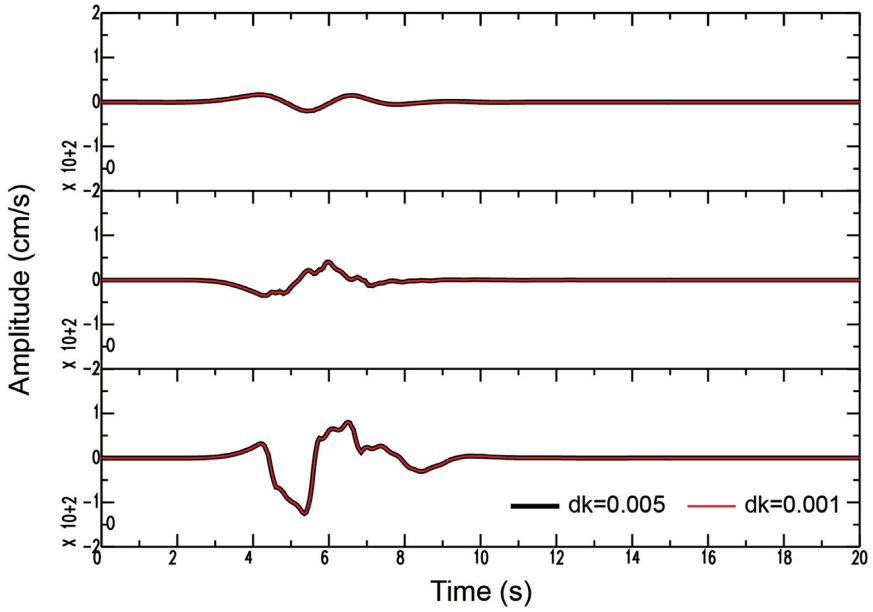

Figure A3. Test of wavenumber increment (dk) in the *F–K* calculation. Black lines indicate the case with dk $= 0.005$ m^{-1} which is applied in all simulations. The red lines are for the case with dk $= 0.001$ m^{-1}. The identical waveforms indicate that dk $= 0.005$ m^{-1} is sufficiently small for the *F–K* simulation.

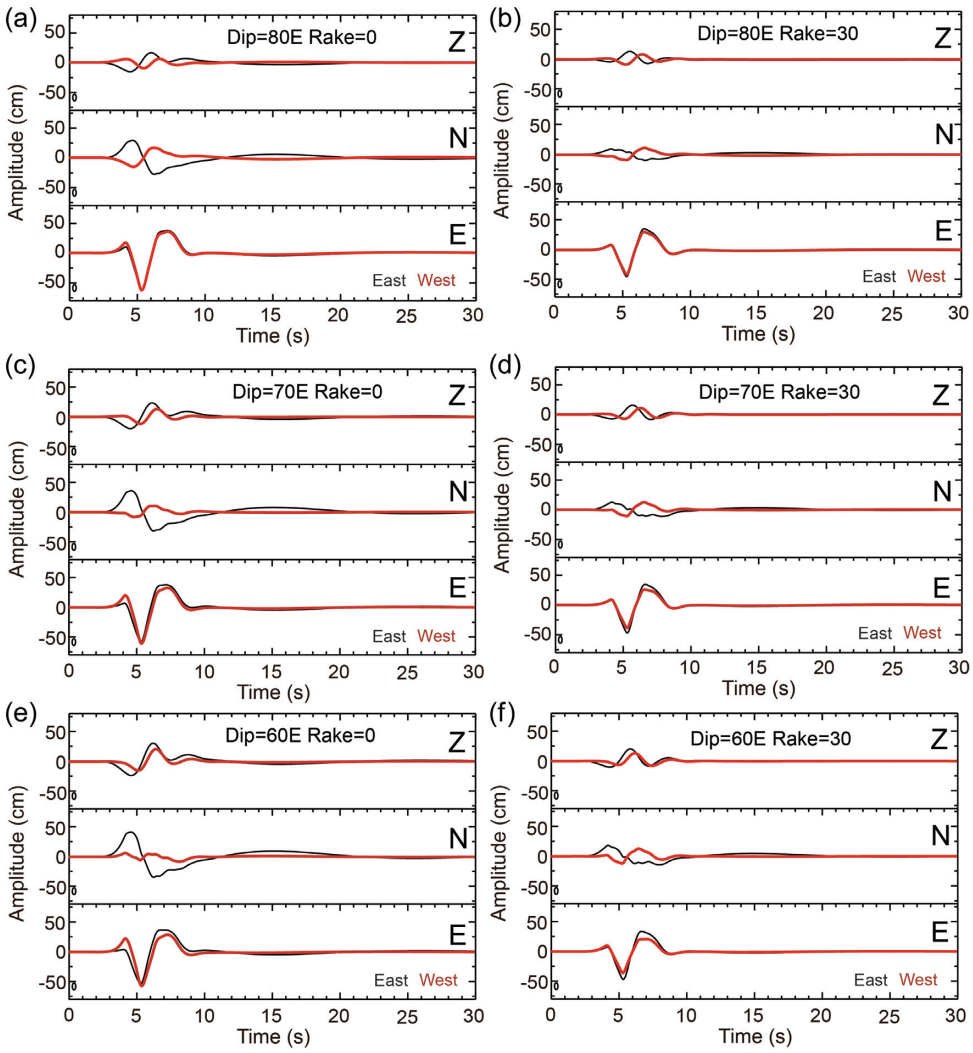

Figure A4. Comparisons of synthetic displacements at the virtual stations on both sides of the line source. The black and red lines are the waveforms for the stations on the east and west sides of the fault, respectively. Different fault geometries of the Milun fault are used: (a) dip angle of 80°E and rake of 0°, (b) dip angle of 80°E and rake of 30°, (c) dip angle of 70°E and rake of 0°, (d) dip angle of 70°E and rake of 30°, (e) dip angle of 60°E and rake of 0° and (f) dip angle of 60°E and rake of 30°.

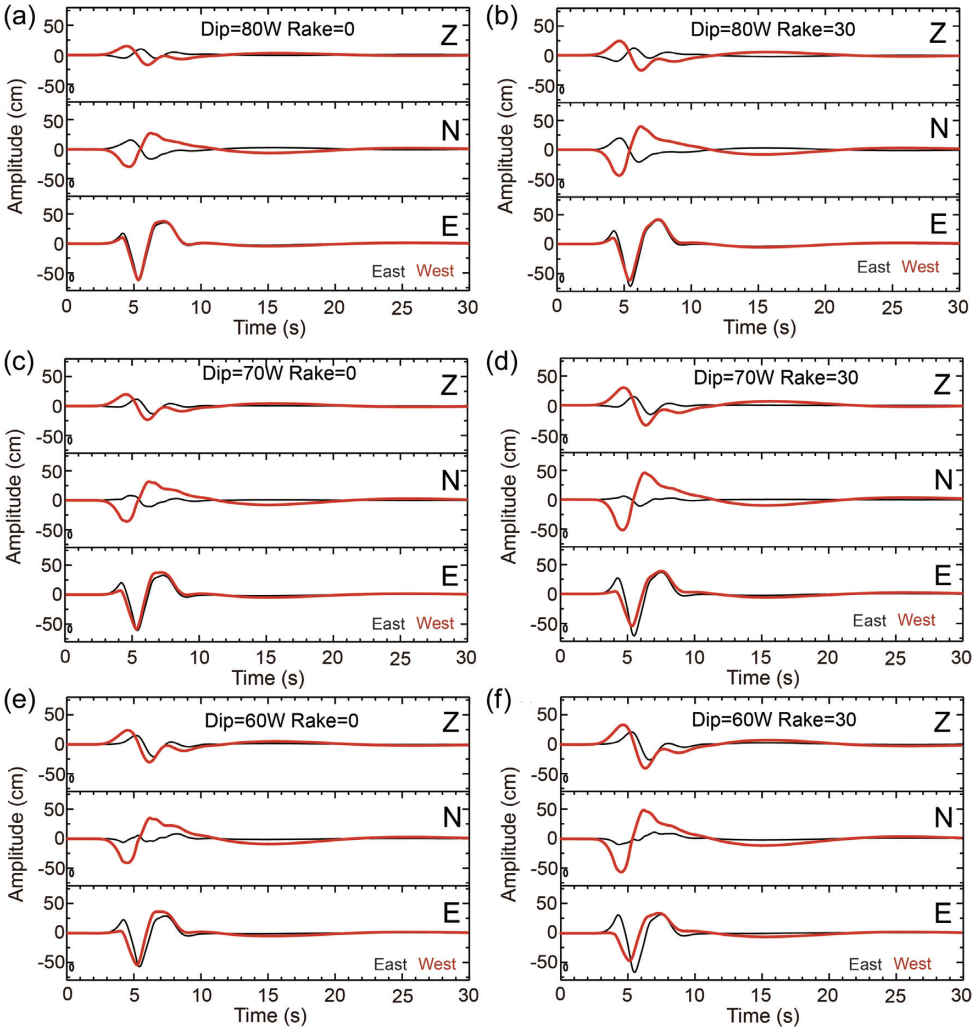

Figure A5. Comparisons of synthetic displacements at the virtual stations on both sides of the line source. The black and red lines are the waveforms for the station on the east and west sides of the fault, respectively. Different fault geometries of the Milun fault are used: (a) dip angle of 80°W and rake of 0°, (b) dip angle of 80°W and rake of 30°, (c) dip angle of 70°W and rake of 0°, (d) dip angle of 70°W and rake of 30°, (e) dip angle of 60°W and rake of 0° and (f) dip angle of 60°W and rake of 30°.

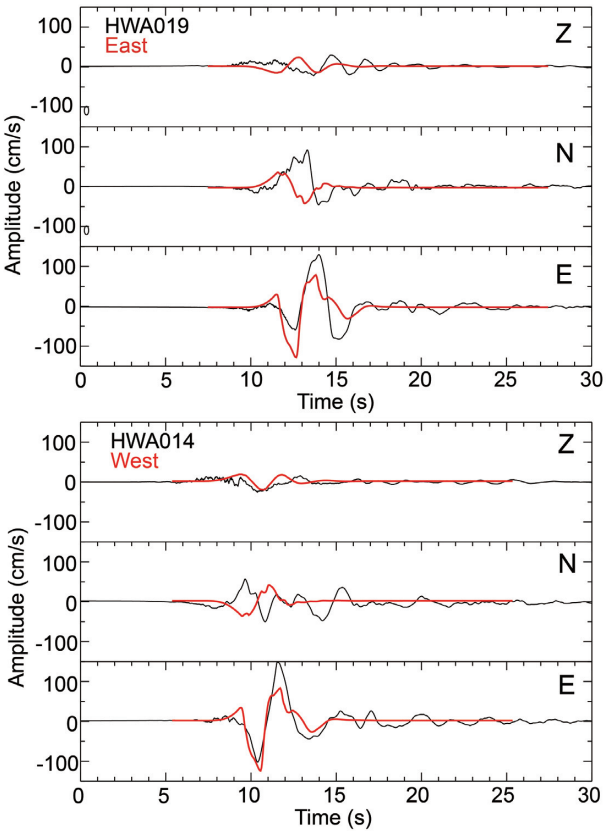

Figure A6. Comparison of the observed velocity ground motions at stations HWA014 and HWA019 (black), located on the west and east sides of the Milun fault, respectively, near the southern end (Fig. 2), with the synthetics (red) computed for the virtual site, W and E (Fig. 8).